ENSO Predictability of a Fully Coupled GCM Model Using Singular Vector Analysis

YOUMIN TANG

Environmental Science and Engineering, University of Northern British Columbia, Prince George, British Columbia, Canada

RICHARD KLEEMAN

Courant Institute of Mathematical Sciences, New York University, New York, New York

SONYA MILLER

Science Applications International Corporation, and NASA Goddard Space Flight Center, Greenbelt, Maryland

(Manuscript received 20 January 2005, in final form 21 July 2005)

ABSTRACT

Using a recently developed method of computing climatically relevant singular vectors (SVs), the error growth properties of ENSO in a fully coupled global climate model are investigated. In particular, the authors examine in detail how singular vectors are influenced by the phase of ENSO cycle—the physical variable under consideration as well as the error norm deployed. Previous work using SVs for studying ENSO predictability has been limited to intermediate or hybrid coupled models.

The results show that the singular vectors share many of the properties already seen in simpler models. Thus, for example, the singular vector spectrum is dominated by one fastest growing member, regardless of the phase of ENSO cycle and the variable of perturbation or the error norm; in addition the growth rates of the singular vectors are very sensitive to the phase of the ENSO cycle, the variable of perturbation, and the error norm. This particular CGCM also displays some differences from simpler models; thus subsurface temperature optimal patterns are strongly sensitive to the phase of ENSO cycle, and at times an east–west dipole in the eastern tropical Pacific basin is seen. This optimal pattern also appears for SST when the error norm is defined using Niño-4. Simpler models consistently display a single-sign equatorial signature in the subsurface corresponding perhaps to the Wyrtki buildup of heat content before a warm event. Some deficiencies in the CGCM and their possible influences on SV growth are also discussed.

1. Introduction

There are generally several forms of errors that limit the skill of ENSO dynamical prediction. They include initial-condition errors and physical-process parameterization model errors as well as unpredictable stochastic forcing by transients in both atmosphere and ocean. Given this, it is of interest in the study of predictability to describe and measure the instabilities of the particular dynamical system under consideration. The usual method for such an analysis is via a linearized version of such dynamical systems. This is thought to be of particular relevance for ENSO because there is much evidence that the system may be only weakly nonlinear in behavior (e.g., Penland and Sardeshmukh 1995; Moore and Kleeman 1998; Tang et al. 2001)

Two common methods often used to explore error growth of a dynamical system include normal mode and Lyapunov vector analysis (see, e.g., Palmer 1999). It has been argued in the literature (e.g., Moore and Kleeman 1999; Chen et al. 1997; Chang et al. 1996; Penland and Sardeshmukh 1995; Thompson and Battisti 2000, 2001) however that the ENSO system may be significantly nonnormal and in that circumstance singular vectors (SVs) are a better indication for short-term (several months) error growth. We adopt this approach here.

The earliest work using SVs to explore the growth of initial condition errors was documented in Lorenz (1965). Over the last decade or so, there has been intensive study of ENSO predictability using SV analysis: by constructing a statistical model analogous to the

Corresponding author address: Youmin Tang, Environmental Science and Engineering, University of Northern British Columbia, 3333 University Way, Prince George, BC, V2N 4Z9, Canada. E-mail: ytang@unbc.ca

original Zebiak and Cane (1987, hereafter ZC) model, Blumenthal (1991) and Xue et al. (1994) studied the optimal growth of initial errors in the ZC model and found that the pattern of SST perturbation favorable to the optimal error growth is very similar to the model ENSO pattern, and that the largest growth rate occurs during spring. Chen et al. (1997) used the Battisti (1988) version of the ZC model to calculate SV and found that the optimal perturbation pattern consists of an east–west dipole in the entire tropical Pacific basin superimposed on a north–south dipole in the eastern tropical Pacific. Xue et al. (1997a,b) and Thompson (1998) also obtained results similar to those in Chen et al. (1997) using the ZC model and the Battisti (1988) coupled model, respectively. Fan et al. (2000) used a different intermediate complexity coupled model from the ZC and Battisti models and found that optimal error growth depends critically on the seasonal cycle and ENSO phase as well as the lead time of prediction. The optimal perturbation pattern of SST has the largest anomalies in the eastern Pacific for the prediction of lead time of 12 months whereas the western Pacific is the most important for the lead time of 3 months. Moore and Kleeman (1996, 1997a,b) extensively examined the dynamics of error growth and predictability in an intermediate-complexity coupled model via analyzing SVs that were computed using a linear-tangent coupled model and its adjoint. They found that the conditions for error growth are favorable in the central Pacific where SSTs are warm, and where changes in SST are sensitive to anomalies of oceanic thermocline. The error growth is also seasonally and ENSO cycle dependent with the largest growth during the spring and the onset of El Niño and the smallest growth during La Niña.

However, all such studies on the optimal error growth of ENSO prediction with SV analysis have been to date limited to intermediate or hybrid (simple atmosphere and OGCM) coupled models. There has been no analysis for ENSO predictability using SVs for a coupled GCM (CGCM), which potentially represents the most realistic physics and dynamics of the observed system. Besides costly computation, a major obstacle that prevents the application of SVs in CGCMs is the fact that the fastest growing modes in such models are invariably due to weather instabilities that are unrelated to the climatically relevant coupled instabilities. Recently a filtering methodology for focusing on the climatically relevant part of the singular vector spectrum has been proposed in Kleeman et al. (2003). This defines the climate response as essentially the ensemble mean response where such an ensemble is generated by very small variations in the atmospheric initial conditions. Such an approach effectively filters out the atmospheric noise but retains the coupled response. This new framework, which we explain further in the next section, enables us to extend previous SV analyses to realistic CGCMs.

In this paper, our particular focus is on investigating the influence of the phase of ENSO cycle and perturbation variables on the error growth. The paper is structured as follows: Section 2 briefly introduces the theoretical framework used to calculate SV in a CGCM. Section 3 describes the coupled general circulation model under study. Section 4 discusses the choice of the variables that are perturbed at the initial time and the prescribed reference trajectories that are used as the basic state to derive linear operators as well as the error norms used to measure prediction error. Section 5 presents primary features of SVs and the influence of phase of ENSO cycle on error growth under three chosen error norms. Finally a summary and discussion can be found in section 6.

2. A theoretical framework for calculating climatically relevant singular vectors for a CGCM

a. Singular vectors

A general dynamical system may be written compactly as

$$\boldsymbol{\Psi}(t) = \mathbf{F}[\boldsymbol{\Psi}(t')], \tag{1}$$

where $\boldsymbol{\Psi}$ is a vector representing system state, and $\mathbf{F}$ is nonlinear operator. For a small perturbation $\boldsymbol{\Theta}$, Eq. (1) can be written as

$$\boldsymbol{\Psi}(t) + \delta\boldsymbol{\Psi}(t) = \mathbf{F}[\boldsymbol{\Psi}(t') + \boldsymbol{\Theta}]. \tag{2}$$

Subtracting Eq. (1) from Eq. (2), we have

$$\delta\boldsymbol{\Psi}(t) = \mathbf{R}\boldsymbol{\Theta}, \tag{3}$$

where the linear operator $\mathbf{R}$ in Eq. (3) is the first-order derivative of $\mathbf{F}$ with respect to $\boldsymbol{\Psi}$ (at the time of t'). It is often called the propagator of Eq. (1) and gives the time evolution of the dynamical system.

Error growth is evidently dependent on the particular measure or norm used to define it. Singular vectors are often sensitive to this choice of error norm. Moore and Kleeman (1996) used energy and enstrophy norms when they calculated SVs whereas other workers have often used the L_2 norm (e.g., Chen et al. 1997; Xue et al. 1997a,b; Thompson 1998; Kleeman et al. 2003). In this work, we adopt the quadratic norm, that is, the predic-

tion error is defined by $\delta\mathbf{\Psi}^{\mathrm{T}}\mathbf{P}^{\mathrm{T}}\mathbf{P}\delta\mathbf{\Psi}$,[1] where the T is transpose, and the $\mathbf{P}$ is a matrix of weights. It is straightforward to choose large weights for $\mathbf{P}$ in regions where we desire to analyze error growth. By definition, we can derive the optimal initial patterns (SVs) giving the largest final error response in our area of interest.

The amplification of the initial perturbation $\mathbf{\Theta}$ over $t - t'$ is, therefore,

$$\lambda^2 = \frac{\delta\mathbf{\Psi}^{\mathrm{T}}\mathbf{P}^{\mathrm{T}}\mathbf{P}\delta\mathbf{\Psi}}{\mathbf{\Theta}^{\mathrm{T}}\mathbf{\Theta}} = \frac{\mathbf{\Theta}^{\mathrm{T}}\mathbf{R}^{\mathrm{T}}\mathbf{P}^{\mathrm{T}}\mathbf{P}\mathbf{R}\mathbf{\Theta}}{\mathbf{\Theta}^{\mathrm{T}}\mathbf{\Theta}}. \quad (4)$$

The vector $\mathbf{\Theta}$ that maximizes λ^2 in Eq. (4) is the first eigenvector of $\mathbf{R}^{\mathrm{T}}\mathbf{P}^{\mathrm{T}}\mathbf{P}\mathbf{R}$. The projection operator $\mathbf{P}$ yields weighted vectors such that $\tilde{\mathbf{R}} = \mathbf{P}\mathbf{R}$. Therefore, the eigenvalues and eigenvectors $\mathbf{E}$ of $\mathbf{R}^{\mathrm{T}}\mathbf{P}^{\mathrm{T}}\mathbf{P}\mathbf{R}$ can be obtained from a singular value decomposition (SVD) of $\tilde{\mathbf{R}}$ (Strang 1988). The first singular value and the corresponding SV represent the greatest error growth rate and the optimal forcing patterns in initial state—the most rapidly evolving and changing modes.

Denoting by λ_1 and $\mathbf{S}_1$ the first singular value and the first SV, we have (Xue et al. 1997a; Fan et al. 2000)

$$\lambda_1\mathbf{S}_1 = \tilde{\mathbf{R}}\mathbf{E}_1.$$

Hence $\lambda_1\mathbf{S}_1$, derived by applying the propagator to the initial pattern, is the corresponding final pattern, where $\mathbf{S}$ is the left vector of SVD of $\tilde{\mathbf{R}}$.

b. Calculation of the linear propagator $\mathbf{R}$

Traditionally, there are two methods to calculate the linear propagator $\mathbf{R}$. One uses the tangent-linear and adjoint model of Eq. (1) to precisely obtain $\underline{R}$ and its singular vectors (e.g., Moore and Kleeman 1996, 1997a b, 1998) and the other is to derive the R through perturbing the forward model Eq. (1) (e.g., Lorenz 1965; Chen et al. 1997; Xue et al. 1994, 1997a; Fan et al. 2000). Both methods have widely been applied to intermediate-complexity coupled models or hybrid coupled models for the study of climate predictability (e.g., Chen et al. 1997; Moore and Kleeman 1996; Thompson and Battisti 2000, 2001). However, there is a fundamental obstacle in applying either to a CGCM as discussed in the introduction: For simplicity consider the first method and consider the perturbation of the initial conditions by a particular climate variable such as SST. It is known that this response is very sensitive to initial conditions in the sense that on climate time scales one will obtain very different results using atmospheric initial conditions differing only very slightly. This highly sensitive response to initial conditions is not just confined to atmospheric variables since one is dealing with a fundamentally coupled system. This effect is, of course, a natural consequence of atmospheric chaos, but obviously it complicates the study of the climate response of the dynamical system. An intuitively appealing unique climate response is provided by an ensemble mean, that is, take a whole series of sensitive responses to initial conditions and simply average them. Interestingly the "ensemble mean" propagator of a linear stochastic differential equation with additive stochastic forcing is exactly the propagator of the system without stochastic forcing. In other words if we were able by some device to remove the stochastic forcing, then the ensemble mean response would provide the appropriate response for the nonstochastically forced system. There are obviously other ways in which a unique/climate response could be defined, however the ensemble mean provides in our view the most intuitively straightforward filtering method (also see Wu et al. 2004). It also corresponds with what happens in intermediate and hybrid coupled models where the response is very close to unique since the atmospheric component gives a unique response to given oceanic forcing. One could also attempt to construct the linearization of a CGCM [such models are actually available for certain models, e.g., the European Centre for Medium-Range Weather Forecasts (ECMWF) system], however one is then faced with a difficult filtering problem when considering the singular vector spectrum since the atmospheric transients have the fastest growth rates and will probably swamp the slower growing climate vectors of interest.

The ensemble mean approach discussed presents practical problems for a CGCM since the model state space is of enormous dimension (typically at least 10^6) and one needs to perturb the system with all dimensions and many times for an ensemble. Obviously this is impractical with present computational power. Fortunately there is considerable evidence from simpler coupled models that the effective state space for ENSO is quite small. We used therefore a well-designed [see Kleeman et al. (2003) for further discussion] reduced space for perturbations. This earlier work showed that the reduced space of correlation EOFs was the most efficient. Previous work has also shown that convergence of results is relatively rapid after 3–5 dimensions and 20–30 ensemble members [Kleeman et al. (2003) provides a detailed discussion on these points].

For calculating $\mathbf{R}$ of a dynamical system, one must first choose a target (denoted by A, e.g., SST) of mea-

[1] The error is originally defined by $\delta\mathbf{\Psi}^{\mathrm{T}}\mathbf{W}\delta\mathbf{\Psi}$, where the $\mathbf{W}$ is a matrix of weights. For a real symmetric $\mathbf{W}$, it can be expressed in terms of the Cholesky decomposition (Fan et al. 2000), that is, $\mathbf{W} = \mathbf{P}^{\mathrm{T}}\mathbf{P}$.

suring prediction errors. Second, the variables that will be perturbed at the initial time (also called perturbation variables hereafter denoting by T_b[2] should be determined. The leading SV of A indicates what kind of the uncertainty in T_b can lead to the fastest error growth for predicting A. In this study, we always use SST to measure the prediction errors. Thus, the procedure of calculating $\mathbf{R}$ and the SV is the same for all cases except that the perturbation EOF modes are derived from an individual perturbation variable.

The detailed procedure for obtaining $\mathbf{R}$ is similar to that described in Kleeman et al. (2003) as follows:

(i) An ensemble of 30 predictions with lead time of 6 months is constructed by randomly perturbing the initial T_b field with 30 "very small" random patterns. The ensemble mean of a specific variable of interest is denoted by $\overline{\mathbf{\Psi}}_0(t)$ (i.e., SST in this study).
(ii) Each of the leading three correlation–EOF modes e_i, of T_b ($i = 1, 2, 3$) are added (with a multiplication factor of 0.1 to ensure linearity) in turn to the initial condition described in (i) and a new ensemble of 30 predictions is produced. The corresponding ensemble means are denoted by $\overline{\mathbf{\Psi}}_i(t)$.
(iii) A reduced-state space matrix version r_{ij} of the propagator R can be obtained from the equation

$$\mathbf{R}\mathbf{e}_i = \overline{\delta\mathbf{\Psi}_i(t)} = \overline{\mathbf{\Psi}}_i(t) - \overline{\mathbf{\Psi}}_0(t) = \sum_{j=1}^{3} r_{ij}\mathbf{e}_j + \text{Residual}, \quad i = 1, 2, 3. \tag{5}$$

It has been found that the residual is generally very small (Kleeman et al. 2003). The climatically relevant singular vectors for CGCMs are thus obtained by SVD for $\tilde{\mathbf{R}}$ as aforementioned. The singular vectors of $\tilde{\mathbf{R}}$ are then projected back to real T_b space using the EOF basis vector expansion.

3. The coupled model

The coupled model used here is the Global Modeling and Assimilation Office Coupled General Circulation Model version 1 (GMAO CGCMv1), developed at the National Aeronautics and Space Administration (NASA) Goddard Space Flight Center. It comprises the NASA Seasonal-to-Interannual Prediction Project (NSIPP) atmospheric model (AGCM), the Poseidon ocean model (OGCM), and Mosaic land surface model (LSM). The NSIPP AGCM has a finite-differenced, primitive equations dynamical core that allows arbitrary horizontal and vertical resolution. It uses a finite-difference C-grid on latitude–longitude coordinates in the horizontal and a generalized sigma coordinate in the vertical. The model resolution used here is $3^\circ \times 3.75^\circ$ in the zonal and the meridional, and 34 sigma layers in the vertical. The top of the model atmosphere is at 10 mb, where we assume $\sigma = 0$. The model details are described in Suarez (1996; also see http://gmao.gsfc.nasa.gov/research/modeling/cgcm/index.php).

The OGCM is a Poseidon quasi-isopycnal ocean model (Schopf and Loughe 1995). It is designed with a finite-difference reduced-gravity formulation that uses a generalized vertical coordinate to include a turbulent well-mixed surface layer with entrainment parameterized according to a Kraus–Turner bulk mixed layer model. The isopycnal region is treated in a quasi-isopycnal fashion, in which layers do not vanish at outcrops, but retain a thin minimum thickness at all grid points. The PP (Pacanowski and Philander 1981) scheme is used to parameterize the subsurface mixing and diffusion. The pressure field is designed with a reduced-gravity formulation. The version used here has a horizontal resolution of $1.25^\circ \times 0.5^\circ$ in the zonal and the meridional direction, and 27 layers in the vertical direction ranging from depths of about 6000 and 8000 m at the equatorial eastern and western Pacific Ocean.

The LSM computes areally averaged energy and water fluxes from the land surface in response to meteorological forcing. The model allows explicit vegetation control over the surface energy and water balances. The land surface scheme is based on the simplified version of the simple biosphere, but extended to a more complicated framework accounting for subgrid variability in surface characteristics through the "mosaic" approach. The model details can be found in Koster and Suarez (1996).

The atmospheric, ocean, and land models are coupled by the Goddard Earth Modeling System, which produces routine experimental ENSO prediction of SST for the tropical Pacific region. The hindcasts during 1981–98 show useful skill (i.e., Niño-3 SST anomaly correlation scores of at least 0.6) for 6–7 months without ocean data assimilation, and the assimilation of altimeter data led to better prediction skills (Rienecker 2000)

4. The choice of the perturbation fields, reference trajectories, and error norm

Before we proceed with SV analysis, some important issues should be first addressed since to a great extent

[2] In this study, the SST and the sea temperature of other two model layers are respectively chosen as the perturbation variables (see section 4a).

they determine SVs and their growth rates, that is, the optimal error growth of predictions. The factors influencing SV include the variables that are perturbed at the initial time, the prescribed reference trajectories that are used as a basic state to derive the propagator R, and the error norm that measures the prediction error.

a. The perturbation variables

The uncertainty in many variables can lead to prediction errors in a realistic coupled model. It is of interest to investigate which variables must be determined most accurately at forecast initialization time to produce the best SST forecast. Using an intermediate-complexity coupled model and energy norm, Moore and Kleeman (1996) found that thermocline information was much more important than SST for SST prediction. Xue et al. (1997a,b) obtained similar conclusions when using the CZ model and L_2 error norm. On the other hand, Fan et al. (2000) and Thompson (1998) concluded that the initial information of both the SST field and the thermocline field is equally important for SST prediction in the tropical Pacific when using two different intermediate-complexity coupled models.

A major interest in this study is to investigate the difference of SVs between intermediate-complexity models and the CGCM. Therefore, we also focus our attention on the sensitivity of the SST prediction error to the uncertainty in SST and in the thermocline at initial state. One good variable to characterize the thermocline displacement is the upper-ocean heat content (HC). However HC is not a model prognostic variable, limiting its SV analysis. For simplicity, we use the subsurface temperature of two model layers for SV analysis. The chosen subsurface layers are model layer 12 and model layer 20, respectively, which cover the model thermocline zone. Displayed in Fig. 1 is the mean depth of the two layers, which was derived from the last 10 yr of a 50-yr model coupling integration. In following discussions, the temperatures of model layers 12 and 20 are denoted, respectively, as T12 and T20. It should be noted that the thermocline displacement changes the temperature in many layers, thus the SVs of T12 and T20 might mainly explore the impact of the uncertainty in two subsurface temperature fields on the SST prediction errors.

b. Reference trajectories

In this study, the ENSO cycle with some seasonal background is used as the reference trajectory for SV analysis. This allows us to examine the influence of the interannual cycle on the error growth in the coupled model. This CGCM has a realistic interannual variability with a period of 3 yr or so. The green line in Fig. 2 shows the variability of SST anomalies (SSTAs) over the Niño-3 region (5°N–5°S, 150°–90°W). As can be seen, the model produces a realistic ENSO oscillation with a range of SSTA from about +2.0° to −2.8°C.

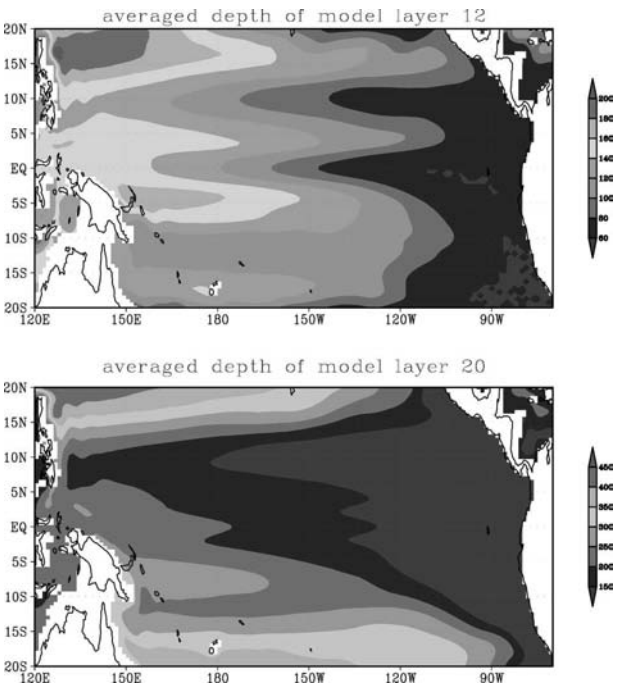

FIG. 1. The mean depth at model layers 12 and 20 averaged over the last 10 yr of a 50-yr coupling integration.

For reasons of computational efficiency, we will choose several typical ENSO phases to perform SV analysis in this study. For generality, we choose five

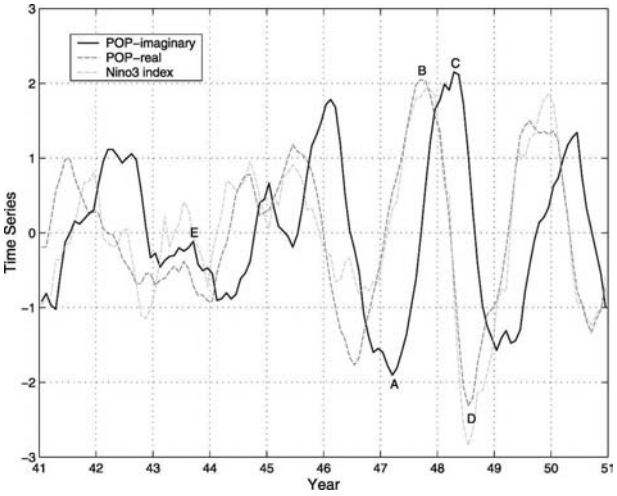

FIG. 2. The time series of the first POP mode of HC, and of the Niño-3 SSTA index.

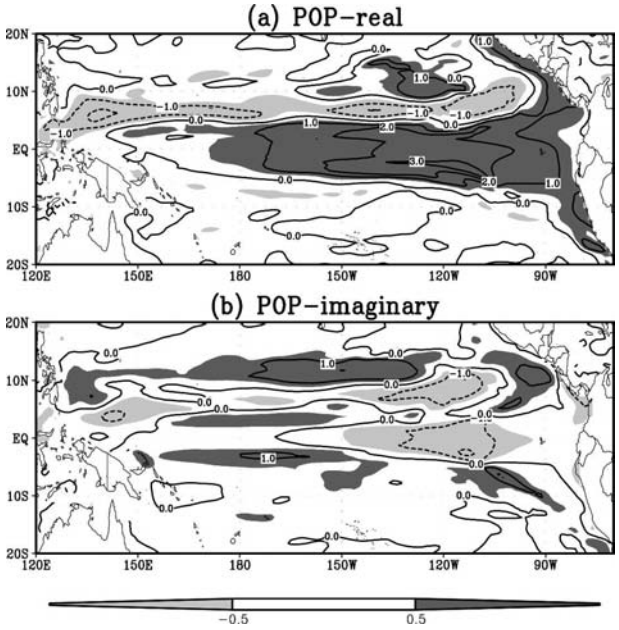

FIG. 3. The (a) real part and (b) imaginary part of the first POP mode of HC.

ENSO phases, that is, the peak of El Niño, the peak of La Niña, the onset of El Niño, the onset of La Niña, and the neutral state.

We use the upper-ocean heat content anomalies (HCAs[3]) to identify ENSO phases because it represents ENSO physics and thermodynamics well. Fluctuations in HCAs are both systematic and significant in the evolution of ENSO, and are thus an effective measure of ENSO phase.

Principal oscillation pattern (POP) analysis (von Storch et al. 1988) was performed on HCAs to identify the typical phases of the ENSO cycle. A dominant ENSO-related POP mode is chosen by the several measures: the oscillation period, variance contribution, and the correlation of the POP coefficients with Niño-3 SSTA index. Displayed in Fig. 2 is its real and imaginary component of the time series. This mode explains 36% of the total variance, with a period of about 26 months. The correlation coefficient of its real time series with Niño-3 SSTA index is 0.88. The spatial patterns of the POP mode are shown in Fig. 3. The real part corresponds to the peak phase of ENSO, while the imaginary part corresponds to the transition phase. The POP characteristics of the CGCM are somehow similar to those found in intermediate-complexity coupled models and hybrid coupled models (e.g., Balmaseda et al. 1994; Kleeman and Moore 1997; Tang et al. 2004), which could be interpreted by the delayed-action oscillator (Battisti 1988), but they also have some differences with the simple models and observations (Latif and Graham 1992). For example, off-equatorial Rossby waves disperse much faster in the equatorial western Pacific in the CGCM than in simple coupled models, so that the Rossby wave signals in Fig. 3a are rather weak compared with strong and apparent "Rossby wave–like" responses characterized in hybrid coupled models, indicating possible differences in dynamics and physics between the CGCM and relatively simple models. A further discussion on the model behavior and the delayed-action oscillator will be presented in section 5a.

The five typical ENSO phases are chosen using the dominant ENSO-related POP mode as shown in Fig. 2. They are, respectively, *B* for the peak of El Niño, *D* for the peak of La Niña, *C* for the onset of La Niña (or post–El Niño), *A* for the onset of El Niño (or pre–El Niño), and *E* for neutral state.

c. The error norm

In this study, one major interest is to obtain the optimal spatial pattern that causes the greatest error growth for a particular region such as Niño-3. This can simply be implemented by SV analysis under a well-defined error norm as discussed in section 2a. For example, we could prescribe the projection operator $\mathbf{P}$ to be diagonal (and equally weighted) for the area of interest and zero elsewhere.

The $\mathbf{P}$ are matrices defined on model space. As discussed in section 2b, a reduced space from leading EOF modes shall be used to derive propagator $\mathbf{R}$ to save the computational cost. To evaluate the prediction error on the reduced space, we have to develop a kernel (norm) $\mathbf{U}$ in the reduced space that is consistent with its counterpart in original model space.

As aforementioned, under the quadratic norm, the prediction error is measured on original space Ω_1 by

$$\|\delta\boldsymbol{\Psi}\|_{\Omega_1} = \delta\boldsymbol{\Psi}^{\mathrm{T}}\mathbf{P}^{\mathrm{T}}\mathbf{P}\delta\boldsymbol{\Psi}. \tag{6}$$

Denoting a reduced space by Ω_2 constructed by EOF leading modes, the projection of $\delta\boldsymbol{\Psi}$ in Ω_2, $\delta\mathbf{A}$ can be obtained by a linear mapping, that is,

$$\delta\mathbf{A} = \mathbf{E}^{\mathrm{T}}\delta\boldsymbol{\Psi}, \tag{7}$$

where $\mathbf{E}$ is base vectors of Ω_2, composed of leading EOF modes $\mathbf{e}_i$ (i = 1, 2 . . .). In reduced space Ω_2, the prediction error should be defined by $\delta\mathbf{A}^{\mathrm{T}}\mathbf{U}\delta\mathbf{A}$, where $\mathbf{U}$ is a weight matrix defined in Ω_2.

[3] Heat content is defined here as the integral of the temperature over the upper 22 model layers, calculated from HC = $(\Sigma_{i=1}^{22} h_i T_i / \Sigma_i h_i)$, where h_i and T_i are, respectively, the thickness and temperature of level *i*.

Combining Eqs. (6) and (7), we have

$$\|\delta\Psi\|_{\Omega_2} = \delta\mathbf{A}^{\mathrm{T}}\mathbf{E}^{\mathrm{T}}\mathbf{P}^{\mathrm{T}}\mathbf{P}\mathbf{E}\delta\mathbf{A}. \quad (8)$$

Hence, the norm in reduced space is $\mathbf{U} = \mathbf{E}^{\mathrm{T}}\mathbf{P}^{\mathrm{T}}\mathbf{P}\mathbf{E}$. For the specific case of L-2 norm, $\mathbf{U} = \mathbf{P}^{\mathrm{T}}\mathbf{P}$ due to the orthogonality of $\mathbf{E}$ and $\mathbf{P}^{\mathrm{T}}\mathbf{P}$ to be proportional to the identity matrix.

5. Singular vector analysis

In this section, we will examine how error growth varies with different phases of the ENSO cycle and different perturbation variables in the CGCM under a prescribed error norm. Our results show that the first singular value (the growth rate) is at least 10 times as much as the second value in all cases considered here, so we only discuss the first singular value and its corresponding vector. The first singular vector represents the initial pattern that will most rapidly grow over the optimal interval. The amplitude of the first singular value provides an indirect measure for the fastest growing rate at which a trajectory perturbed a small distance from the original model trajectory at the initial state will diverge from the original trajectory when averaged over the optimal interval.

a. Predicting SST over the Niño-3 region

To precisely predict SST variations in the Niño-3 or Niño-3.4 (5°N–5°S, 170°–120°W) regions is particularly important in ENSO prediction because of the direct definition of El Niño. It is meaningful to explore what is the optimal perturbation mode that could lead to the fastest error growth of Niño-3 SSTA prediction. As argued in Fan et al. (2000), this is also equivalent to the following question: To predict SST in the Niño-3 region, where is the most important initial oceanic temperature information located?

Prescribing P to be diagonal with unit entries for Niño-3 region and zero elsewhere, we perform the SV analysis. Table 1 shows the first singular values for five different ENSO phases and three different perturbation variables, respectively. As can be seen, the first singular values vary greatly with different ENSO phase and different perturbation variables. Compared with SST and T12, the uncertainty in T20 is less favored for error growth, which might be consistent with such a fact that the thermal structure of upper ocean plays a dominant role on the ENSO oscillation since layer 20 is located near the bottom of the thermocline layer (see Fig. 1).

To compare the relative importance of error growth caused by initial uncertainty in SST and in T12 could shed light on which initial uncertainty is more important for predicting SST anomalies of the equatorial eastern Pacific. Layer 12 approximately lies at the upper thermocline layer. As shown in Table 1, the error growth is larger for the initial uncertainty in SST except when the prediction starts from the neutral state, in which case the initial uncertainty in T12 has a larger error growth. This suggests that initial uncertainty in SST is equally important with, or even more important than, the subsurface temperature T12 for predicting Niño-3 SSTA for most initial states, especially for the onset of El Niño. This result is consistent with those shown in Thompson (1998) and Fan et al. (2000), but different from those in Moore and Kleeman (1996) and Xue et al. (1997a,b), which showed that subsurface information has more influence on the evolution of the system than initial SST information.

TABLE 1. The first singular value optimized at 6 months as the function of ENSO phase and the depth of perturbation, with the norm unity weight in Niño-3.

ENSO phase (start time)	Surface	Layer 12	Layer 20
El Niño (September)	19.13	14.45	11.99
La Niña (August)	5.66	5.40	4.03
Neutral state (February)	14.37	21.16	1.82
Onset La Niña (April)	12.16	5.6	4.40
Onset El Niño (March)	107.29	12.13	8.04

Figure 4 shows the time–longitude distributions of SSTA, zonal wind, and heat content anomalies along the equator during years 41 to 50 in a 50-yr model coupling integration. Figure 4 might reasonably explain why the initial uncertainty in SST plays a significant role in the error growth of predictions in the CGCM. As shown in Fig. 4a, SSTA exhibits an obvious feature of westward propagation, which is not consistent with the observation (Fig. 5b). This is due mainly to the contribution of the zonal advection of SST, and could be explained by the mechanism of surface layer feedbacks (Neelin et al. 1998). In Fig. 4b, the alternating westerly and easterly wind anomalies lie over the central and western equatorial Pacific and to the west of the SST anomalies (Fig. 4a). In the surface layer feedback, for the warm episodes of ENSO, the surface layer eastward current and downwelling anomalies occur under the westerlies, thus tending to reinforce the original anomaly, shifting it westward by the mean temperature advection by the anomalous currents in the surface layer and contributing to the westward propagation of SSTA. To the east of the original warm anomaly, easterly winds tend to create cold anomalies by this mecha-

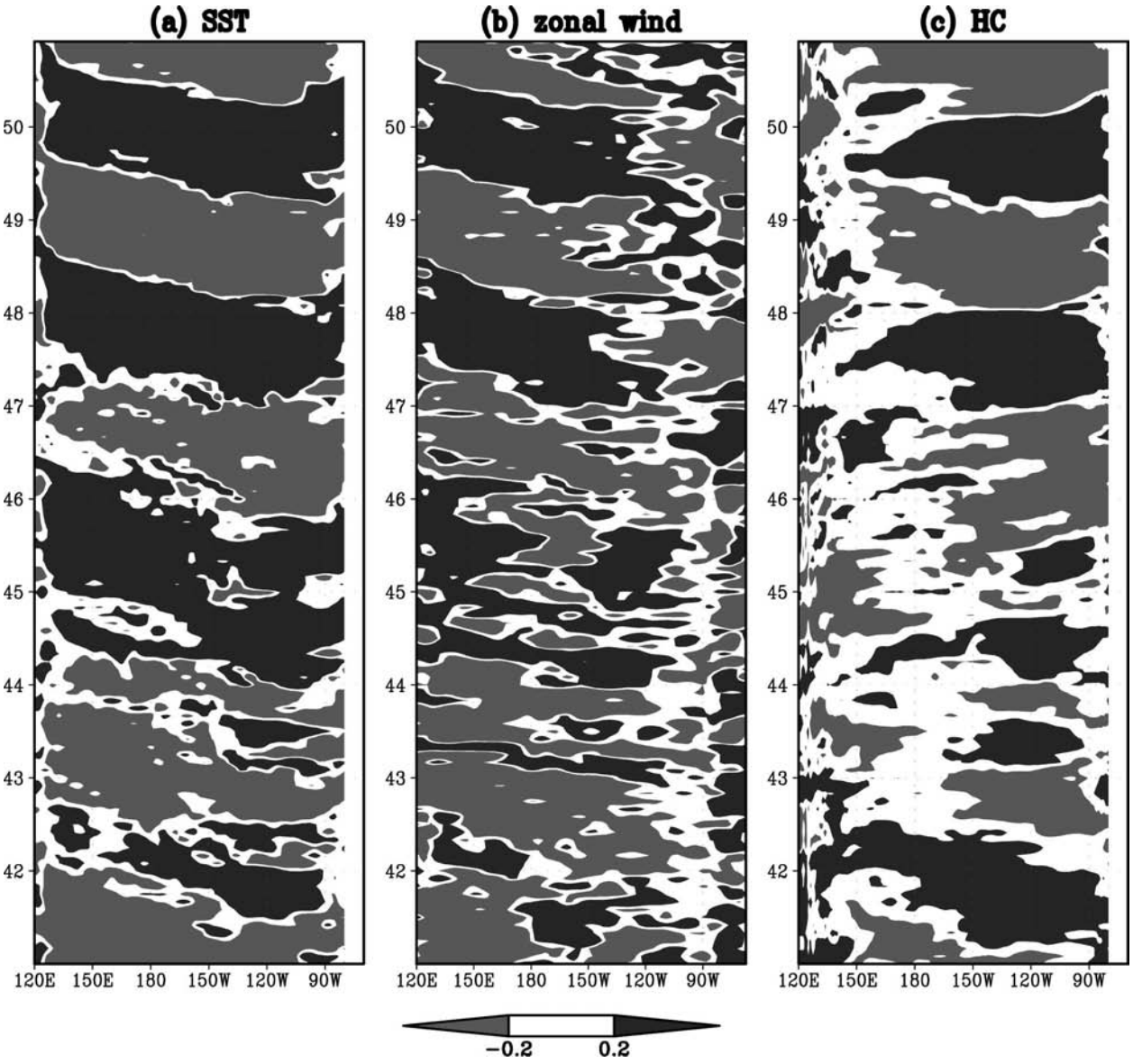

FIG. 4. Time–longitude diagrams along the equator for (a) SSTA, (b) the zonal wind (× 100), and (c) the heat content anomaly of the upper 22 model layers. The units are °C in (a) and (c) and N m^{-2} in (b). The annual cycle has been removed prior to plotting.

nism, potentially resulting in a westward-propagating succession of warm anomalies (Neelin et al. 1998). For the cold episodes of ENSO, analogous arguments can be applied to explain the westward propagation of the cold anomalies.

A significant feature in the variation of observed heat content is its eastward propagation along the equator (Fig. 5a), which could be explained by thermocline dynamics (e.g., Latif and Graham 1992; Tang 2002). This feature has been captured by many intermediate-complexity models (e.g., Zebiak and Cane 1987; Tang 2002). However, the eastward propagation of HCA is not significant in the CGCM, as shown in Fig. 4c. This suggests that the subsurface T12 and T20 contribution to SST variability over the east Pacific might be not so significant as the horizontal advection, and might be underestimated in this CGCM.

Figures 6 and 7 are, respectively, the variations in the observed and modeled HCA and SSTA along 8°N. The observed HCA displays an obvious westward propagation of Rossby waves at the off-equator region, which is absent in the modeled counterpart. In addition, an in-

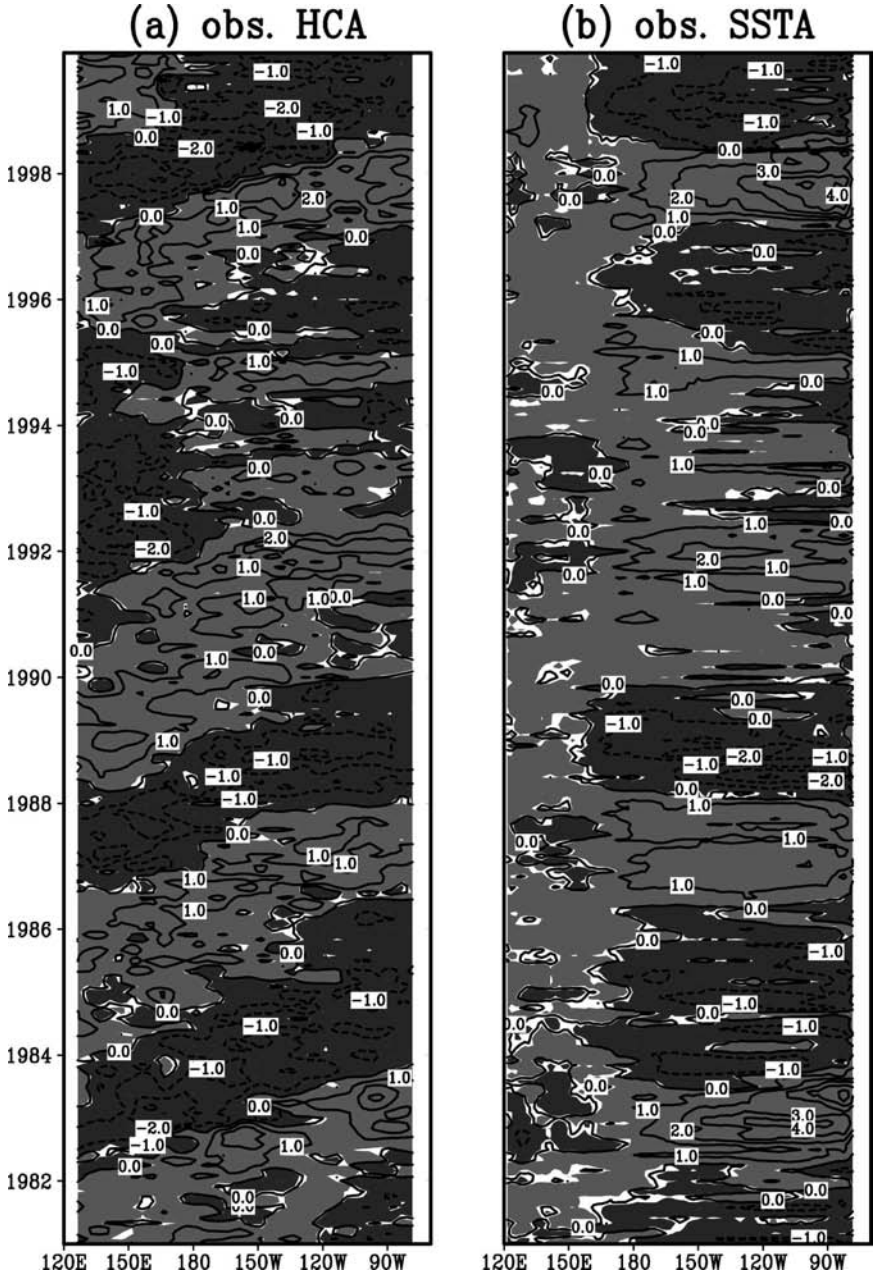

FIG. 5. Time–longitude diagrams along the equator for observed (a) HCA and (b) SSTA.

teresting feature in the observed SSTA is that the 1982/83 El Niño seemingly appeared to propagate eastward along the off-equator region, which is probably caused by a diagonal stretch of warm SST between Indonesia and Baja California that migrated south.

Therefore, the reason why the perturbation in SST can lead to faster error growth than in T12 and T20 in the model might be due to 1) the significant contribution of zonal advection of surface temperature to SSTA variability in this model and 2) the relative weak role of T12 and T20 to SST variations. The former was suggested by a recent work of Yuan and Rienecker (2003). They found that SST assimilation can improve the model simulation of temperature advection significantly and produce an estimate of the sea surface heat flux that is consistent with the model dynamics and thermodynamics.

Another noticeable feature in Table 1 is that the error growth depends on the phase of the model ENSO cycle for all situations. For example, the perturbation in

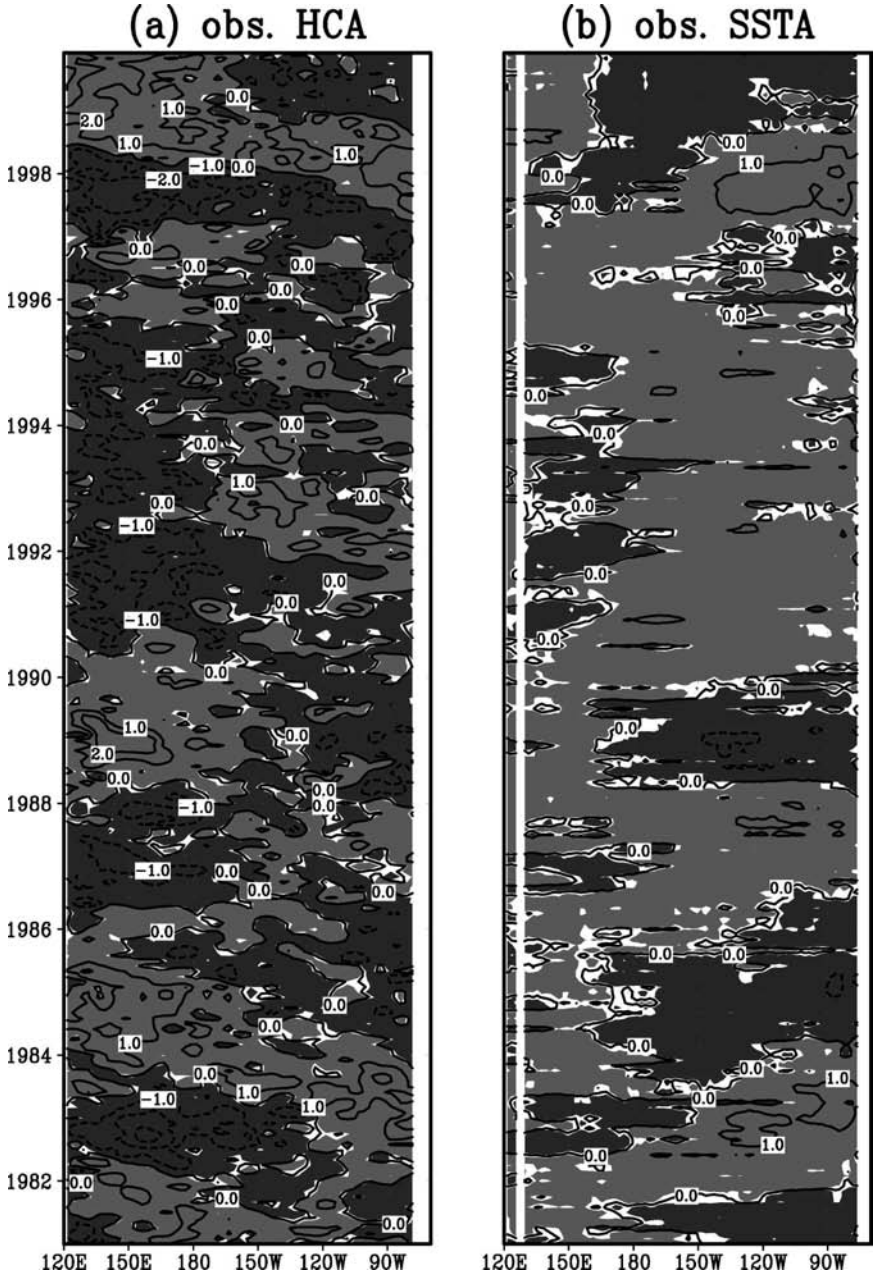

FIG. 6. Same as in Fig. 5, but along 8°N.

SST leads to the largest error growth during the onset of El Niño, and the smallest during the peak of La Niña, whereas the perturbation in T12 leads to the largest error growth during the neutral state and the smallest during the peak of La Niña. In general, the error growth is larger during the onset and peak phase of El Niño than during the onset and peak phase of La Niña, suggesting that El Niño may be less predictable than La Niña in this CGCM. These features are in good agreement with the results obtained from intermediate coupled models (e.g., Xue et al. 1997a,b; Moore and Kleeman 1996, 1997a,b). Moore and Kleeman (1997a,b) explored in detail the mechanism responsible for the variation of SV with the ENSO cycle using an intermediate coupled model. They argued that the surface-driven deep penetrative atmospheric convection is an important driving force for perturbation in the real atmosphere over the western and central tropical Pacific. During the onset and peak phase of El Niño, the central Pacific warms, creating conditions more favorable for

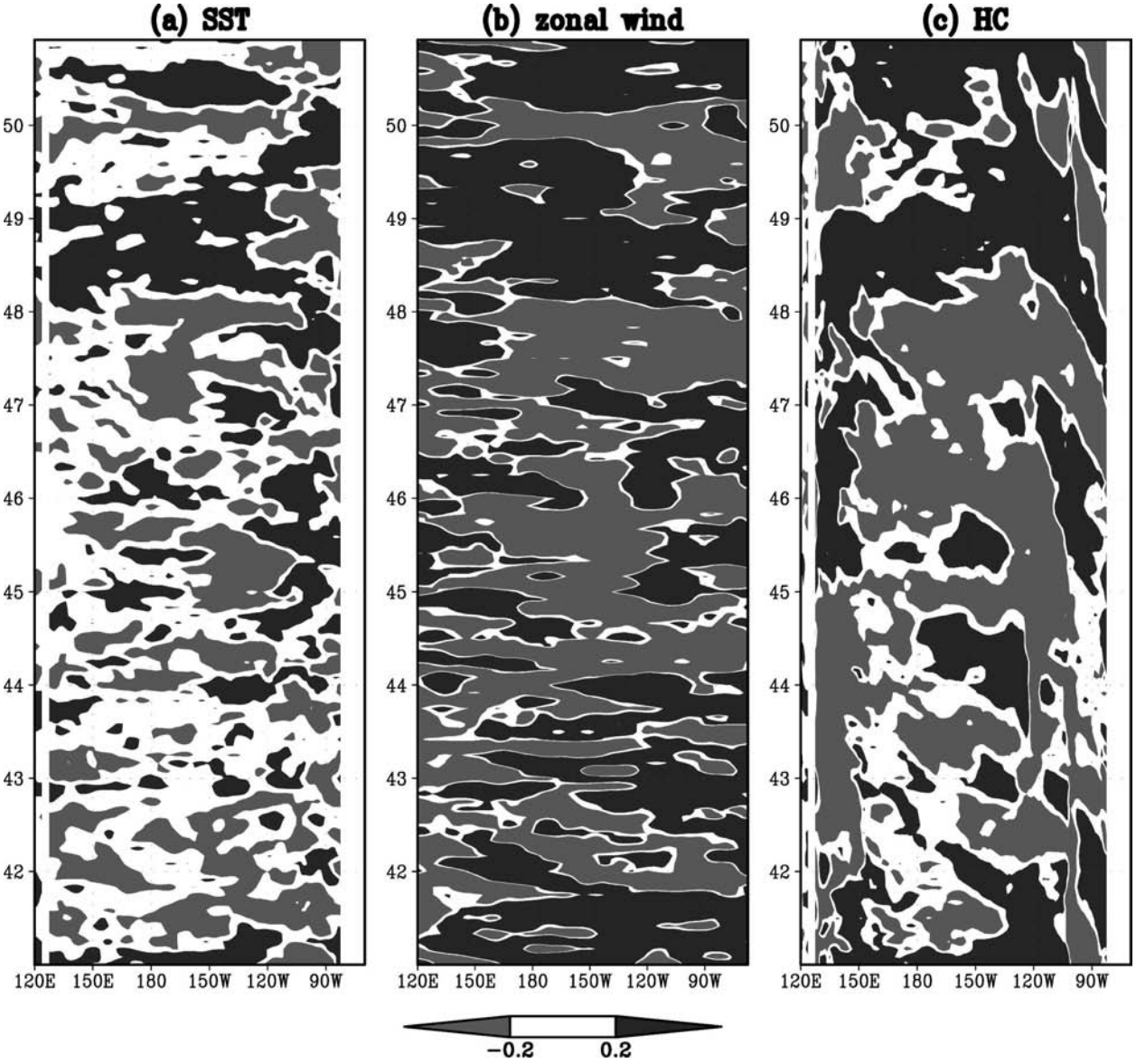

FIG. 7. Same as in Fig. 4, but along 8°N.

deep penetrative convection in the atmosphere. During the onset and peak phase of La Niña, the western Pacific begins to cool and the western Pacific warm-pool begins to recede westward. In the central Pacific, this creates conditions unfavorable for deep penetrative convection, and the inherent ability of all SVs to grow there declines. However this mechanism might not work for this coupled model since the first singular vector in the CGCM shows that the equatorial eastern Pacific is the area most favored for perturbation growth, as shown in Fig. 8a. In Moore and Kleeman (1996, 1997a,b) the western and central parts of the Pacific Ocean are the the areas most favored for error growth. In the Zebiak and Cane model (Chen et al. 1997; Xue et al 1997a,b) and the hybrid coupled model in Fan et al. (2000), SV action is also primarily confined to the central and eastern Pacific. Figure 8a suggests that the surface-driven deep penetrative convection might not play the first important role to strengthen the initial perturbation in SST or in subsurface T12 and T20 in this CGCM. Instead, the mechanism responsible for error growth in the CGCM may be one mixed SST–ocean dynamics mode (see below discussions).

Shown in Figs. 8b,c is the optimal pattern of zonal wind and heat content associated with the first SV of SST for the phase of onset of El Niño and the pertur-

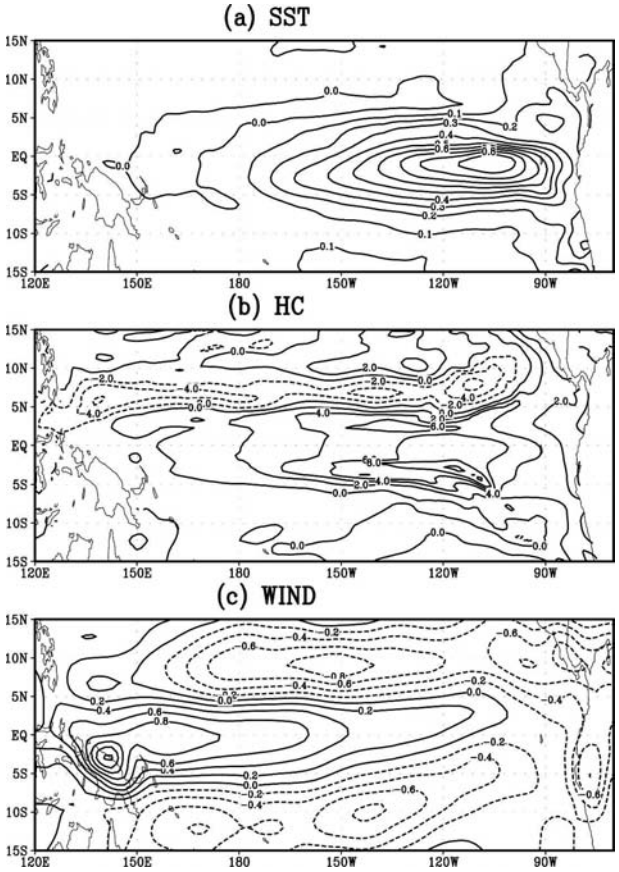

FIG. 8. (a) The first SV mode of SST starting from the phase of onset of El Niño with SST as perturbation variable; (b) the HC pattern associated with the optimal SST structure of (a); (c) same as in (b), but for the zonal wind stress.

bation on SST. The associated patterns of zonal wind and HC were computed as below,

$$\mathrm{APU}(x, y) = \sum_{t=1}^{n} \mathbf{U}(x, y, t)\mathrm{PC}(t),$$

$$\mathrm{APHC}(x, y) = \sum_{t=1}^{n} \mathrm{HC}(x, y, t)\mathrm{PC}(t), \qquad (9)$$

where PC is the time series of the first SV projected onto SSTA fields. APU and APHC are the zonal wind and HC pattern that usually appears when the first SV of SST appears. As can be seen, the spatial patterns in Fig. 8 are somehow similar to the typical delayed-action oscillator diagram but also show considerable differences from it (e.g., Balmaseda et al. 1994; Tang 2002). In a typical delayed-action oscillator diagram, the large zonal HC gradient occurs at the central equatorial Pacific, weakening the upwelling there and intensifying the warm Kelvin waves propagating eastward, whereas large westerly wind anomalies prevail over the central equatorial Pacific associated with the eastward-propagating equatorial Kelvin wave. In such a diagram, the location of large HC gradient and the westerly wind anomalies are two crucial elements to dominate the propagation of subsurface information and adjust ENSO cycle. Obviously, Fig. 8 shows a different structure, with the large HC gradient in the eastern Pacific and the large westerly wind anomalies in the west. The structure of Fig. 8 may infer a mixed SST–ocean dynamics mode (Neelin and Jin 1993): the strong westerly will shoal the thermocline in the west and deepen the thermocline in the east to balance the wind stress, creating the warm anomalies in the subsurface in the east; the warm anomalies are carried to the surface by upwelling, leading to the SSTA warm anomalies there. Meanwhile, the strong westerly wind transfers surface warm water from the west to the east. In the western Pacific, SSTA westward propagation is dominated by surface layer feedbacks due to the deep thermocline there as discussed above.

Figure 9 is the final pattern of the SV after a 6-month evolution. Comparing Fig. 8 with Fig. 9 reveals a significant growth of the SV, as indicated by the singular value in Table 1.

Unlike the singular value, the sensitivity of the first SV variation to the phase of the ENSO cycle is more complicated. When the perturbation was applied to the SST and the T12, the derived SV was not sensitive to different phases of the ENSO cycle. In the both cases, the leading SVs are characterized by a common spatial pattern similar to Fig. 8a for all phases of ENSO cycle. This is consistent with the results found in simpler coupled models (e.g., Moore and Kleeman 1996; Xue et al. 1997a,b; Chen et al. 1997; Fan et al. 2000). However, when the perturbation was applied to T20, the first SV exhibits some disparities among different initial phases. Shown in Fig. 10 is the first SV for five different ENSO phases with the perturbation onto the T20. While the initial conditions start at neutral state, the peak of La

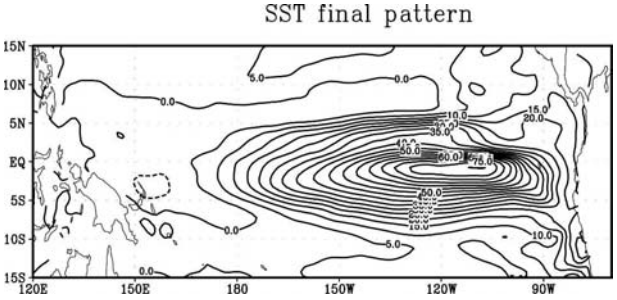

FIG. 9. The final pattern of the first SV denned in Fig. 8 after a 6-month evolution.

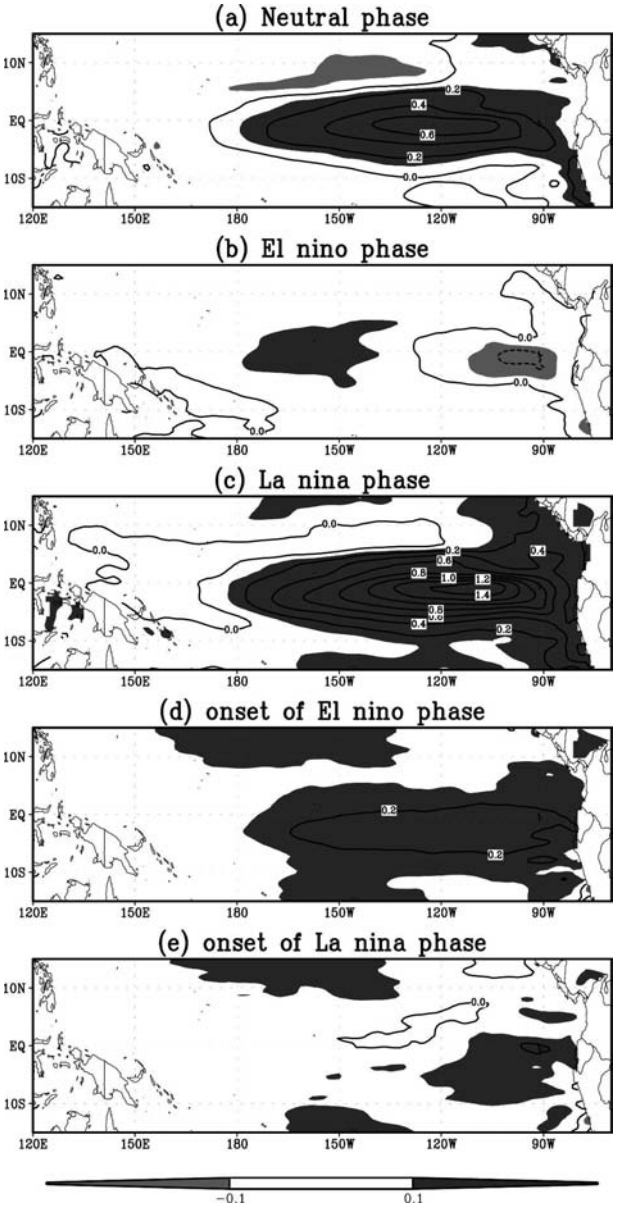

FIG. 10. The first SV modes of SST, calculated respectively from five different ENSO phases. The perturbation variable is T20 and the norm unity weight is given in the Niño-3 area.

Niña and the onset of El Niño, the first SVs also show a spatial pattern similar to Fig. 8a; whereas the initial conditions are the peak El Niño and onset of La Niña; however, the first SVs show little spatial variability. The latter suggests that the error growth is sensitive to the uncertainties in T20 over a large domain of tropical Pacific. On the other hand, when predictions are initialized from other phases of the ENSO cycle, the error growth is mainly affected by the uncertainties in T20 over the equatorial east Pacific.

b. Predicting SST over the entire tropical Pacific and Niño-4

In this section, we will present the results of SVs with the error norm defined by the entire tropical Pacific. This allows us to investigate where the most important initial oceanic temperature information is located for predicting SST in the entire tropical Pacific. For this purpose, we define weight matrix **P** to be diagonal with unit entries for the 20°N–20°S, 120°E–90°W region and zero elsewhere. Table 2 is the first singular value optimized at 6 months derived from the new error norm. As can be seen, the first singular values here are very close to those in Table 1. Table 2 also reveals many features similar to Table 1: 1) the first singular value in Table 2 also depends on the phase of the model ENSO cycle; 2) the error growth is larger during the onset or peak phase of El Niño than during the onset or peak phase of La Niña; 3) the uncertainty in SST and T12 favors the prediction error growth more than that in T20; and 4) the initial uncertainty in SST is equally important with, or even more important than, that in T12 and T20 at most initial states, especially at the onset of the El Niño phase.

Like the singular values, the SVs derived from the error norm also bear a striking similarity to those obtained from the error norm of Niño-3 discussed in section 5a (not shown), that is, 1) SV is not sensitive to different phases of the ENSO cycle for the perturbation of SST and the T12, characterized by a typical El Niño–like pattern, as in Fig. 8a; 2) for the perturbation of T20, the first SV exhibits some disparities among different initial phases, as in Fig. 10.

The striking similarity of singular values and SVs between the two error norms indicates that the error growth for predicting the entire tropical Pacific SST is probably due to that for predicting Niño-3 SST. This might be explained by the fact that the SST interannual variability is relatively small in the western Pacific compared to that in the eastern Pacific so that the SST in the eastern Pacific varies more easily than SST in the west. Thus, no matter what perturbation is applied, under uniform weighting, SVs for the entire Pacific will be

TABLE 2. Same as in Table 1, but with the norm unity weight in the entire tropical Pacific.

ENSO phase (start time)	Surface	Layer 12	Layer 20
El Niño (September)	23.3	16.7	14.1
La Niña (August)	7.1	6.2	4.6
Neutral state (February)	18.6	25.0	2.2
Onset La Niña (April)	14.1	14.6	9.4
Onset El Niño (March)	127.4	7.8	5.0

TABLE 3. Same as in Table 1, but with the norm unity weight in Niño-4.

ENSO phase (start time)	Surface	Layer 12	Layer 20
El Niño (September)	6.2	4.1	4.2
La Niña (August)	1.6	1.6	1.0
Neutral state (February)	4.3	6.7	1.0
Onset La Niña (April)	3.6	0.5	1.4
Onset El Niño (March)	32.5	4.1	2.7

dominated by what happens in the east since the perturbation has more impact on the eastern Pacific. These results are very consistent with those obtained using an intermediate hybrid coupled model (Fan et al. 2000). A further investigation on this issue is to calculate SVs with the error norm defined by the Niño-4 (5°N–5°S, 160°E–150°W) region.[4]

Table 3 is the first singular value calculated under the error norm of Niño-4. Comparing Table 3 with Tables 1 and 2 reveals that the singular values for the prediction of Niño-4 SST are almost all a little less than one-third of those for the prediction of Niño-3 or the entire tropical Pacific SST. This is in good agreement with the results shown in Table 1 and Table 2, that is, the error growth is much slower for the prediction of Niño-4 SST than for the prediction of Niño-3 SST, so that the latter almost dominates the error growth for the prediction of the entire tropical Pacific SST.

One interesting result obtained under the error norm of Niño-4 is that the first SV is somewhat sensitive to the initial ENSO phases as shown in Fig. 11, which is in contrast to the first SV under the Niño-3 norm and the entire tropical Pacific norm. In general, the first SV has two different kinds of spatial structure. The first is very similar to Fig. 8a in section 5a, that is, the equatorial eastern Pacific is the region most favorable for the error growth. This kind of pattern appears at the initial phase of neutral state, onset of El Niño, and peak of La Niña. The second kind of spatial structure of the first SV appears at the initial phase of the peak of El Niño and onset of La Niña. As can be seen, this kind of SV is characterized by an east–west dipole along the equator in SST field. Such a dipole was also found to be the SST optimal in several simpler coupled models (e.g., Kleeman et al. 2003; Xue et al. 1997a,b).

However when the perturbation is applied to T12 and T20, the first SV is insensitive to the reference trajectory except that the largest-amplitude center somewhat shifts with different ENSO phases (Fig. 12).

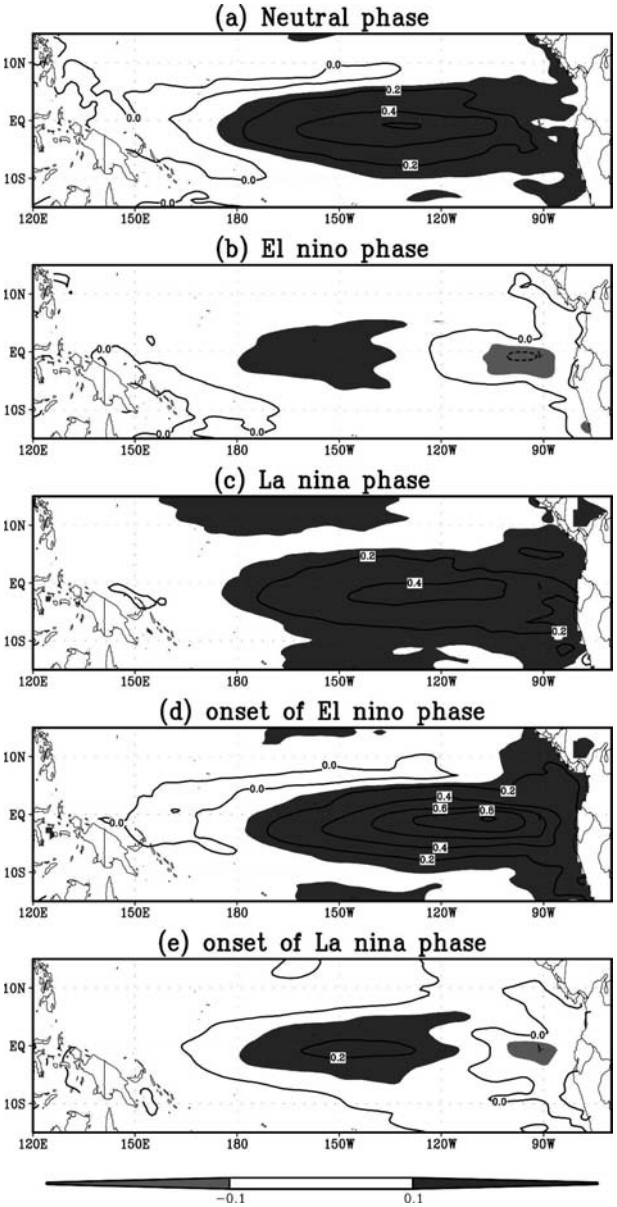

FIG. 11. The first SV modes of SST, calculated from five different ENSO phases, respectively. The perturbation variable is SST and the norm unity weight is given in the Niño-4 area.

The patterns are very similar to those discussed in section 5a, that is, the eastern Pacific Ocean is most favorable for the error growth.

In summary, the results shown above indicate that the eastern Pacific is a crucial region most often favored for error growth. The warm anomalies in the equatorial central and eastern Pacific are a common feature for the optimal perturbation in many models when the error norm is chosen in a form of L-2, Niño-3, or energy growth.

[4] We define weight matrix **P** to be diagonal with unit entries for the Niño-4 region and zero elsewhere.

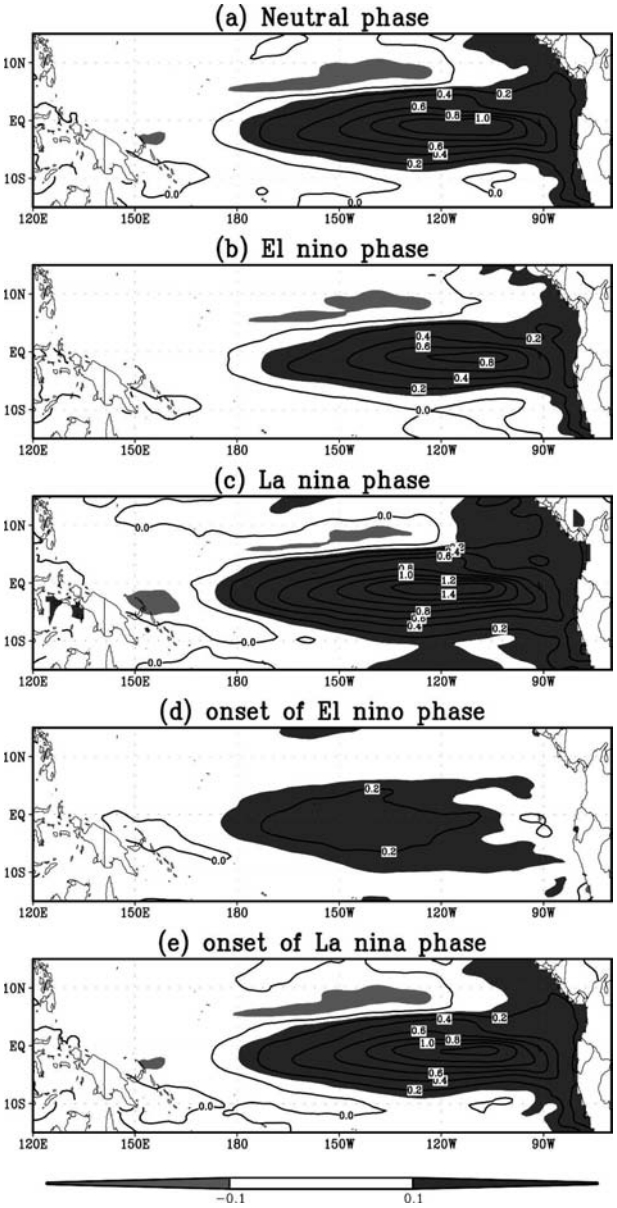

FIG. 12. Same as in Fig. 11, but the perturbation variable is T12.

6. Summary and discussion

Over last decade, there has been an increased interest in understanding ENSO prediction using SVs since it describes in a linear sense the optimal error growth within predictions. SVs of the coupled system have been widely studied using a hierarchy of ENSO models from statistically derived models (e.g., Xue et al. 1994; Penland and Sardeshmukh 1995) and intermediate-complexity coupled models (e.g., Chen et al. 1997; Moore and Kleeman 1996, 1997a,b; Thompson and Battisti 2000; Xue et al. 1997a,b; Fan et al. 2000) to hybrid coupled models (e.g., Moore et al. 2003). However SV analysis has not been applied to a CGCM simply because there was not an adequate technique available for such an analysis. The coupled models display tropical interannual variability that differs considerably from model to model, which could potentially lead to significant differences in the structure and growth rates of SV.

In this paper, we applied a recently developed technique to examine the influence of the model ENSO cycle on SV growth under several specified error norms—the Niño-3 norm, the entire basin norm, and the Niño-4 norm. The different norms were chosen for identifying the areas most favored for the error growth for the prediction of SST of the specified region. The optimal growth interval is chosen to be 6 months since this period has usually the fastest error growing rate and is of practical interest. The perturbation was applied to three different model layers: surface, layer 12, and layer 20; and to five different ENSO phases: peak of El Niño, onset of El Niño, neutral, peak of La Niña, and onset of La Niña.

The results show that the singular-value spectrum is dominated by one singular vector for all cases. The error growth of prediction can be strongly influenced by the phase of the ENSO cycle and the variables of perturbation. Compared to SST and T12, the uncertainty in T20 causes less error growth in all SST predictions. The initial uncertainty in SST is as equally important as T12 and T20 for Niño-3, Niño-4, and the entire basin SST prediction. These findings hold for most initial states of predictions, especially for the initial state of the onset of El Niño. In general, the large growth factors of the fastest-growing singular vectors occur during the onset and the peak of El Niño, whereas relatively small growth factors occurs during the onset and the peak of La Niña. This suggests that El Niño maybe be less predictable than La Niña.

Compared to large variations of the first singular value with the phase of ENSO cycle and the variables of perturbation, the first SV pattern is not very sensitive to changes in ENSO phase and the variables subject to perturbation. This is especially obvious when the norm is chosen to be the Niño-3 norm or the entire tropical norm. Under either norm, one dominant singular vector similar to that in many intermediate models (e.g., Xue et al. 1997a; Fan et al. 2000) and in the observation (Penland and Sardeshmukh 1995) is found. In this optimal pattern, the eastern and central parts of the Pacific Ocean are the areas most often favored for the error growth by the singular vectors. Under the choice of the Niño-4 norm, two dominant singular vectors are found: one is similar to that of the Niño-3 norm and the

other shows an east–west dipole along the equator with major weighting located in the eastern and central Pacific. These results indicate that to predict SST anomalies using this CGCM in both the eastern and the western Pacific 6 months ahead, the important initial upper-ocean temperature information is located mainly in the eastern Pacific. This finding was also documented by Fan et al. (2000) using a simple hybrid coupled model. However there is a large-scale structure located in the Northern Hemisphere subtropical intertropical convergence zone (ITCZ) region in the first SV of the observed SST that is absent in the leading SV of the CGCM like all intermediate and hybrid coupled models.

One interesting result obtained in this study is that the initial information in SST plays more significant roles than that in the temperatures of other two subsurface layers (i.e., T12 and T20) for predicting the tropical Pacific SST. It seemingly contradicts some work that holds that subsurface information is more important for ENSO prediction (e.g., Latif and Graham 1992; Ji et al. 1998), although some simpler models also have similar conclusions (e.g., Fan et al. 2000; Thompson 1998). Several reasons are probably responsible for this: (i) T12 and T20 may not represent subsurface information well. For example, T20 lies around the bottom of the thermocline and has little contribution to SST variabilities in the east equatorial Pacific. (ii) The results may represent the reality reasonably well. There are two popular hypotheses responsible for ENSO oscillations (Neelin et al. 1998): one is subsurface feedback, called delayed-action oscillator, and the other one is the surface layer feedback associated with strong SST zonal advection. The interannual variability in the CGCM could in fact be explained by a mixed mode of subsurface feedback and surface layer feedback (see section 5a). (iii) The subsurface temperature has a strong linear relation with SST in the tropical Pacific (Tang et al. 2004) so the uncertainty in subsurface temperature maybe be able to be resolved and represented by the uncertainty in SST. ENSO is a coupled mode in the tropical Pacific. SST plays a significant role in the coupling process. In this sense, the results might reasonably reflect the importance of SST in the coupling process. Of course, the results might be only model dependent, and result from some deficiencies of the model in physics and dynamics. More work is required to identify the truth.

Several concerns should be born in mind. First, the SV is computed based on five different phases of the ENSO cycle, which are from five different calendar months; thus the results present in this paper might include some seasonal influence. However the seasonal influence should be relatively small since the chosen calendar months approximately fall into two groups, each consisting of adjacent calendar months, that is, February–April and August–September. We believe that the large differences within the same group should be due mainly to the influence of phases of the ENSO cycle. Second, when calculating the SV, for simplicity we give equal weight to all analysis errors and use simple geographical projection operators for $\mathbf{P}$, as in some previous work (e.g., Chen et al. 1997; Thompson 1998). There is no a priori reason to assume that analysis errors have equal weight over all grids and variables of perturbation. One more realistic strategy is to calculate the analysis error covariance using some specific technique, as in Fan et al. (2000). In addition, because of the expensive computational cost, we only choose five typical phases of model ENSO cycle and examine their influence on SV growth. Nevertheless this exploratory work has shed light on the effect of the phase of ENSO cycle on the SV growth in a CGCM model and has obtained some new findings. In particular, the derived optimal perturbation patterns could allow us to effectively generate ensemble prediction for this CGCM model. Also, the results reported in this paper have implications for the initialization of seasonal forecast of this CGCM. For example, the finding that the uncertainty in SST can lead to faster error growth than that in T12 and T20 suggests the importance of SST assimilation in this coupled model. Our recent work (Tang et al. 2004; Tang and Kleeman 2002) indeed showed that the assimilation of SST can significantly improve the prediction skill of Niño-3 SSTA.

Acknowledgments. This work was supported by Canadian Foundation for Climate and Atmospheric Sciences Grant GR-523 and NASA Grant NAG5-9871.

REFERENCES

Balmaseda, M. A., D. L. T. Anderson, and M. K. Davey, 1994: ENSO prediction using a dynamical ocean model coupled to statistical atmospheres. *Tellus,* **46A,** 497–511.

Battisti, D. S., 1988: Dynamics and thermodynamics of a warming event in a coupled tropical atmosphere–ocean model. *J. Atmos. Sci.,* **45,** 2889–2919.

Blumenthal, M. B., 1991: Predictability of a coupled ocean–atmosphere model. *J. Climate,* **4,** 766–784.

Chang, P., L. Ji, H. Li, and M. Flügel, 1996: Chaotic dynamics versus stochastic processes in El Niño-Southern Oscillation in coupled ocean-atmosphere models. *Physica D,* **98,** 301–320.

Chen, Y.-Q., D. S. Battisti, T. N. Palmer, J. Barsugli, and E. S. Sarachik, 1997: A study of the predictability of tropical Pacific SST in a coupled atmosphere–ocean model using singular vector analysis: The role of the annual cycle and the ENSO cycle. *Mon. Wea. Rev.,* **125,** 831–845.

Fan, Y., M. R. Allen, D. L. T. Anderson, and M. A. Balmaseda, 2000: How predictability depends on the nature of uncertainty in initial conditions in a coupled model of ENSO. *J. Climate,* **13,** 3298–3313.

Ji, M., D. W. Behringer, and A. Leetmaa, 1998: An improved coupled model for ENSO prediction and implications for ocean initialization. Part II: The coupled model. *Mon. Wea. Rev.,* **126,** 1022–1034.

Kleeman, R., and A. M. Moore, 1997: A theory for the limitation of ENSO predictability due to stochastic atmospheric transients. *J. Atmos. Sci.,* **54,** 753–767.

——, Y. Tang, and A. Moore, 2003: The calculation of climatically relevant singular vectors in the presence of weather noise. *J. Atmos. Sci.,* **60,** 2856–2867.

Koster, R., and M. Suarez, 1996: The influence of land surface moisture on precipitation statistics. *J. Climate,* **9,** 2551–2567.

Latif, M., and N. E. Graham, 1992: How much predictive skill is contained in the thermal structure of an oceanic GCM? *J. Phys. Oceanogr.,* **22,** 951–962.

Lorenz, E. N., 1965: A study of the predictability of a 28-variable atmospheric model. *Tellus,* **17,** 321–333.

Moore, A. M., and R. Kleeman, 1996: The dynamics of error growth and predictability in a coupled model of ENSO. *Quart. J. Roy. Meteor. Soc.,* **122,** 1405–1446.

——, and ——, 1997a: The singular vectors of a coupled ocean-atmosphere model of ENSO, Part I: Thermodynamics, energetics and error growth. *Quart. J. Roy. Meteor. Soc.,* **123,** 953–981.

——, and ——, 1997b: The singular vectors of a coupled ocean-atmosphere model of ENSO, Part II: Sensitivity studies and dynamical interpretation. *Quart. J. Roy. Meteor. Soc.,* **123,** 983–1006.

——, and ——, 1998: Skill assessment for ENSO using ensemble prediction. *Quart. J. Roy. Meteor. Soc.,* **124,** 557–584.

——, and ——, 1999: Stochastic forcing of ENSO by the intraseasonal oscillation. *J. Climate,* **12,** 1199–1220.

——, J. Vialard, A. Weaver, D. L. T. Anderson, R. Kleeman, and J. R. Johnson, 2003: The role of air–sea interaction in controlling the optimal perturbations of low-frequency tropical coupled ocean–atmosphere modes. *J. Climate,* **16,** 951–968.

Neelin, J. D., and F.-F. Jin, 1993: Modes of interannual tropical ocean–atmosphere interaction—A unified view. Part II: Analytical results in the weak coupling limit. *J. Atmos. Sci.,* **50,** 3504–3522.

——, D. S. Battisti, A. C. Hirst, F.-F. Jin, Y. Wakata, T. Yamagata, and S. Zebiak, 1998: ENSO theory. *J. Geophys. Res.,* **103,** 14 261–14 287.

Pacanowski, R., and S. Philander, 1981: Parameterization of vertical mixing in numerical models of the tropical oceans. *J. Phys. Oceanogr.,* **11,** 1443–1451.

Palmer, T. N., 1999: Predicting uncertainty in forecast of weather and climate. *Rep. Prog. Phys.,* **63,** 71–116.

Penland, C., and P. D. Sardeshmukh, 1995: The optimal growth of tropical sea surface temperature anomalies. *J. Climate,* **8,** 1999–2024.

Rienecker, M., 2000, The NASA seasonal-to-interannual prediction project (NSIPP) progress report. NASA Goddard Space Flight Center, 27 pp.

Schopf, P., and A. Loughe, 1995: A reduced-gravity isopycnal ocean model: Hindcasts of El Niño. *Mon. Wea. Rev.,* **123,** 2839–2863.

Strang, G., 1988: *Linear Algebra and Its Applications.* Harcourt Brace Jovanovich, 442 pp.

Suarez, M., 1996: Dynamical aspects of climate simulations using the GEOS General Circulation Model. NASA Tech. Memo. 104606, Vol. 10, 71 pp.

Tang, Y., 2002: Hybrid coupled models of the tropical Pacific—I: Interannual variability. *Climate Dyn.,* **19,** 331–342.

——, and R. Kleeman, 2002: A new strategy for SST assimilation for ENSO prediction. *Geophys. Res. Lett.,* **29,** 1841, doi:10.1029/2002GL014860.

——, W. W. Hsieh, B. Tang, and K. Haines, 2001: A neural network atmospheric model for hybrid coupled modelling. *Climate Dyn.,* **17,** 445–455.

——, R. Kleeman, and A. Moore, 2004: SST assimilation experiments in a tropical Pacific Ocean model. *J. Phys. Oceangr.,* **34,** 623–642.

Thompson, C. J., 1998: Initial conditions for optimal growth in a coupled ocean–atmosphere model of ENSO. *J. Atmos. Sci.,* **55,** 537–557.

——, and D. S. Battisti, 2000: A linear stochastic dynamical model of ENSO. Part I: Development. *J. Climate,* **13,** 2818–2883.

——, and ——, 2001: A linear stochastic dynamical model of ENSO. Part II: Analysis. *J. Climate,* **14,** 445–466.

von Storch, H., T. Bruns, I. Fischer-Bruns, and K. Hasselmann, 1988: Principal Oscillation Pattern analysis of the 30–60 day oscillation in a GCM equatorial troposphere. *J. Geophys. Res.,* **93,** 11 022–11 036.

Wu, Z., E. K. Schneider, and B. P. Kirtman, 2004: Causes of low frequency North Atlantic SST variability in a coupled GCM. *Geophys. Res. Lett.,* **31,** L09210, doi:10.1029/2004Gl019548.

Xue, Y., M. A. Cane, S. E. Zebiak, and M. B. Blumenthal, 1994: On the prediction of ENSO: A study with a low order Markov model. *Tellus,* **46A,** 512–528.

——, ——, and ——, 1997a: Predictability of a coupled model of ENSO using singular vector analysis. Part I: Optimal growth in seasonal background and ENSO cycle. *Mon. Wea. Rev.,* **125,** 2043–2056.

——, ——, ——, and T. N. Palmer, 1997b: Predictability of a coupled model of ENSO using singular vector analysis. Part II: Optimal growth and forecast skill. *Mon. Wea. Rev.,* **125,** 2057–2073.

Yuan, D., and M. M. Rienecker, 2003: Inverse estimation of sea surface heat flux over the equatorial Pacific Ocean: Seasonal cycle. *J. Geophys. Res.,* **108,** 3247, doi:10.1029/2002JC001367.

Zebiak, S. E., and M. A. Cane, 1987: A model El Niño–Southern Oscillation. *Mon. Wea. Rev.,* **115,** 2262–2278.